Available online at www.sciencedirect.com
SCIENCE DIRECT®
ELSEVIER
International Journal of Multiphase Flow 30 (2004) 565–583
International Journal of Multiphase Flow
www.elsevier.com/locate/ijmulflow

Entrainment of gas in the liquid film of horizontal, annular, two-phase flow

Daniel J. Rodríguez, Timothy A. Shedd *

Multiphase Flow Visualization and Analysis Laboratory, Department of Mechanical Engineering, University of Wisconsin-Madison, 1500 Engineering Drive, Madison, WI 53706, USA

Received 20 October 2003; received in revised form 29 April 2004

Abstract

A backlit digital imaging technique was used to obtain images of bubbles within the liquid film of adiabatic air–water horizontal annular flow. A digital image processing algorithm that isolated bubble contours from other flow features was implemented. The bubble entrainment statistics showed that the bubble size distribution within the liquid film was exponential, and the parameters of the distribution were observed to be dependent on air flow rate and essentially independent of liquid flow rate. The bubble data, together with fluorescent imaging of waves on the liquid film, indicated that gas entrainment in the film was primarily controlled by air flow rate and wave behavior. This was confirmed by the existence of a consistent Weber number based on the maximum observed bubble diameter and disturbance wave velocity.

Keywords: Bubble sizing; Image processing; Gas entrainment; Disturbance waves; Annular flow; Gas absorption; Flow visualization; Film thickness

1. Introduction

In the study of two-phase flow in pipes, discussions regarding entrainment often refer to liquid droplets traveling in the gas or vapor core of annular two-phase flow. The opposite case, that is, bubbles traveling in the liquid film, appears to be just as frequent and suitable for detailed characterization. Bubble entrainment has been qualitatively documented in the existing literature. Jacowitz and Brodkey (1964) documented entrainment in cross cut images of the liquid film for air/water horizontal annular flow. Cooper et al. (1964) used a two-color piped-light illumination

* Corresponding author. Tel.: +1-608-265-2930; fax:+1-608-262-8464.
E-mail address: shedd@engr.wisc.edu (T.A. Shedd).

0301-9322/$ - see front matter
doi:10.1016/j.ijmultiphaseflow.2004.04.011

technique that also detected entrained bubbles and clearly distinguished them from droplets. Arnold and Hewitt (1967) reported the presence of considerable amounts of entrained bubbles in backlit images of the liquid film for air/water vertical annular flow. More recently, Hewitt et al. (1990) presented images of liquid in annular flow illuminated in a manner that clearly displayed entrained bubbles. Through the use of high-speed cine film, they also documented what appeared to be a gas entrainment event at the leading edge of a wave. Other researchers, Thorncroft and Klausner (1997) for example, have documented the presence of bubbles in adiabatic annular flows of pure fluids.

Mesler (1976, 1977) constructed a theory for convective flow boiling heat transfer based on bubbles in the liquid film that originate from mechanical rather than thermal sources. In this work, he noted the potential for the generation of so-called secondary nucleation sites through the entrainment of vapor bubbles with droplet impacts and the trapping of a small amount of vapor during the collapse of a large bubble at the liquid surface. That this theory has been accepted as a possibility by some (Thome, 1995) and challenged by others (Sun and Hewitt, 2001) suggests that the role of entrained vapor in convective boiling warrants additional investigation.

Although previous work has qualitatively documented the presence of entrained bubbles, their size distribution has not been quantified. Size distribution and concentration variations with respect to liquid and gas flow rate, as well as with the circumferential position around the tube, are explored in the present study as a first step towards an assessment of the potential role of bubble entrainment in the heat and mass transfer behavior of horizontal annular flow. The experiments focus on the flow mechanics and bubble statistics of a horizontal, adiabatic air/water system using 70 different annular flow conditions. In addition, the role played by disturbance waves and vapor shear in the entrainment and breakup of bubbles is discussed with the aid of cross-sectional images of the film obtained through fluorescence imaging.

2. Experimental Setup

2.1. Flow loop

The setup shown in Fig. 1 was used for all the statistical measurements. Compressed air and filtered water, both at 20 °C, were combined in a mixing tee. Water entered the air current through multiple 3 mm holes drilled in a regular pattern over the extent of the tube surface enclosed by the tee. The flow was allowed 384 L/D ($L = 5.8$ m) of straight tube length (15.1 mm ID) to develop before reaching the visualization region. The effects of flow within the mixing tee are minimized by allowing this distance before visualizing the flow. The possible effect of the mixing tee geometry on entrainment was studied by inverting the air and water inlets at the tee. No substantial changes in the flow were observed from this alternative mixing setup.

A square cross section, clear acrylic box was fitted over the PVC tube at the viewing section, and the gap was filled with an oil that has an index of refraction almost identical to that of clear PVC. This setup minimizes distortions caused by the curvature of the tube wall. The air/water flow exiting the test section passed into a flow separator, and the water was recirculated from a holding tank using a variable speed drive peristaltic pump fitted with a pulse dampener.

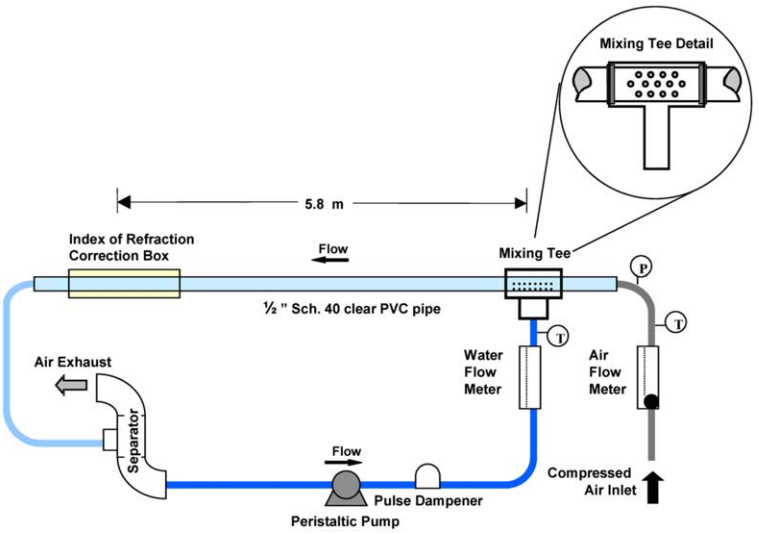

Fig. 1. Air/water flow loop schematic.

The tubing carrying water from the separator to the mixing tee was also clear and it was frequently and carefully inspected for bubbles. Only a small number of randomly occurring bubbles were detected after the separator or the pulse dampener while in steady state operation. When the level in the liquid reservoir or pulse dampener was low, a significant number of bubbles appeared before the mixing tee, and testing was stopped until maintenance on the apparatus was completed. Thus, these extraneous sources of air bubbles can be considered negligible.

The current setup allows measurable water flow rates ranging from 0.2 to 1.5 l/min and air flow rates ranging from 200 to 700 l/min. Variable area flowmeters were employed for measuring the water and air flow rates; only flow rates corresponding to graduations marked by the manufacturer on the meters (i.e., 200, 300 l/min, etc.) were used to ensure the highest accuracy and repeatability. These flowmeters have manufacturer-specified accuracies of 3% of full scale (0.045 l/min) and 2% of full scale (28 l/min) for the liquid and air models, respectively. The air flowmeter was verified to within 5% of the indicated flow over its entire range using an insertion thermal flow meter with a NIST-traceable calibration.

2.2. Image acquisition

A Nikon D100 Digital SLR camera with a 6.1 megapixel resolution was used for gathering the data presented below. The required magnification was achieved using a Nikon MicroNikkor 60 mm f/2.8D macro lens and a Tamron 2X teleconverter. The shutter speed was set at 1/200 s and the aperture at f/11. It should be noted that the use of a 2X teleconverter makes the macro lens two f-stops slower and doubles the focal length. Thus, when estimating the depth of field of this optical system, a 120 mm focal length and an f/22 aperture should be used. For the CCD sensor used in the D100, the circle of confusion diameter is 20 μm. With an object distance of 17 cm (as measured from the detector location), the depth of field is thus calculated to be 0.5 mm. This

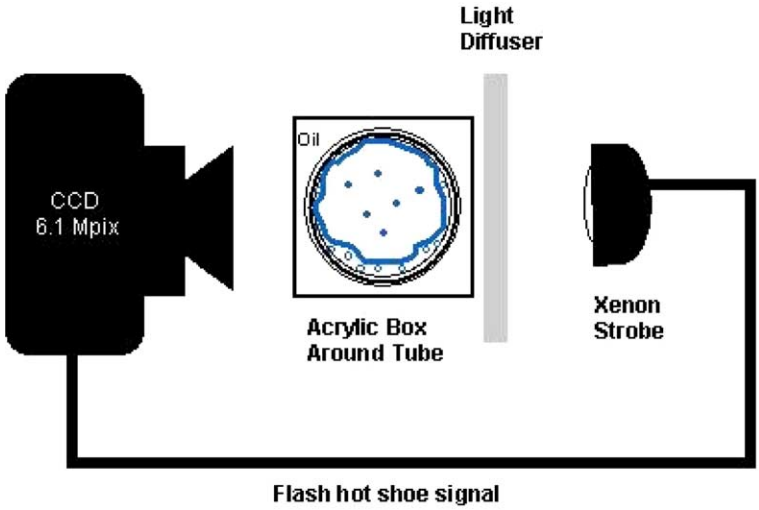

Fig. 2. Setup for backlit images.

depth of field was also directly measured by moving the camera on a translation stage while observing the range over which small marks on the tube surface remained in focus.

The illumination may be described in general as a diffuse transmitted light system, a schematic of which is presented in Fig. 2. The hot shoe flash signal from the camera was used to trigger a xenon strobe light, diametrically opposed to the surface of the tube viewed by the camera. The strobe light produced light pulses of approximately 0.03 ms. This short time, not the shutter speed, was what determined the exposure time, making it short enough to avoid significant image blur at the observed flow velocities. The success of the subsequent image processing relies on providing an even backlighting. A diffuser was installed between the strobe light and the tube for this purpose. Several materials were tested as diffusers, including ground glass, opaque polymers and glossy paper sheets. The best results were obtained using two sheets of glossy paper (44 lb. bond coated on one side) with the glossy side facing the tube.

2.3. Experimental procedure

The experimental matrix consisted of 5 air flow rates and 14 liquid flow rates (reported below as superficial velocities: $U_{\text{superficial}}$ = volumetric flow rate/tube cross-sectional area based on ID). One hundred images were captured for each flow setting. The Region of Interest (ROI) that was actually processed from each raw image frame was restricted in height in order to avoid curvature distortion of the vertical scale and to maintain an evenly illuminated background. The ROI depicts an area of 12.5×3.9 mm at a resolution of 4.2 μm/pixel.

In general, the greatest difficulty in capturing images was obtaining a good focus on the contours of bubbles traveling within the liquid film. A good focus should provide enough sharpness for the automated detection of the bubble contours. Even with the use of a rather small aperture (f/22), a very narrow depth of field (approximately 0.5 mm) results since the focal length is large and the object is very close to the lens. Therefore, no parts of the liquid film traveling along the

opposite side of the tube, or any entrained liquid droplets in the vapor core, were visible in the images. Moreover, the liquid on the opposite side of the tube enhances the desirable light diffusion. The dimensions of the waves create lenses with very short focal lengths, thus actually improving the diffusion of the light. The out-of-focus waves, droplets and bubbles are small and tend to act as scatterers (which cause additional diffusion).

A translation stage fitted with a micrometric screw was used to couple the camera body to a tripod. Very finely trimmed radial translation control was achieved with this setup, and it yielded optimal focus control.

2.4. Image processing

Each set of 100 images was batch processed using a script implemented with National Instruments IMAQ™ Vision Builder V.6.0 software. Details on the standard image processing operations used can be found in Gonzalez and Woods (1993). The complete script consists of 19 steps. The raw images were cropped, converted to 8-bit grayscale, and the histogram was stretched to enhance contrast.

The first step in the processing is an image threshold that produces a binary image in which the darker regions of the frame are separated from the light background. Dark regions include both the circular edges produced by bubbles (bubble contours) and the higher crests of the air–water interface. A contour is defined here as the finite width boundary of a closed curve. The width of this dark edge around the bubble image is finite because of optical dispersion phenomena at the bubble interface. Some of the smaller bubble contours were thin and not completely closed. A contour closing procedure (a dilation followed by an erosion) was used to increase the number of closed bubble outlines by filling in the gaps in nearly continuous boundaries that would otherwise go undetected by the subsequent image processing operations.

Next, the Heywood circularity factor is used as a criterion for finding nearly circular contours. This factor is the ratio of a contour perimeter to the perimeter of a circle with the identical area. Thus, a circle has a Heywood circularity factor of one. Contours with a Heywood circularity factor ranging from 1 to 1.20 were accepted. Those contours consisting of less than 20 pixels were discarded since they were judged too small to resolve accurately. If this finite boundary were 1 pixel thick, the diameter corresponding to a 20 pixel contour would be approximately 6 pixels. However, the actual thickness of the boundary was usually more than 1 pixel, which results in 3 or fewer pixels left to resolve the diameter; this was considered an insufficient amount.

The image that resulted from the foregoing processing was stored in a memory buffer. The steps described above were applied again in an identical cycle on the raw image, but using a different threshold value optimized for the detection of additional small bubbles located along the brighter horizontal centerline of the ROI; a significant number of these are ignored by the first threshold due to the large difference in contrast. After eliminating duplicate bubbles, the results of this second processing cycle were added to the contours stored in the buffer containing the results of the first cycle.

Fig. 3 shows the main steps for the image processing of a base film image (i.e., an image of the base liquid film between waves). The first image in the figure shows the raw grayscale image. The second image was obtained after thresholding. Note that the darker areas of the frame are still included. After the Heywood circularity criterion was applied and the smaller pixel clusters were

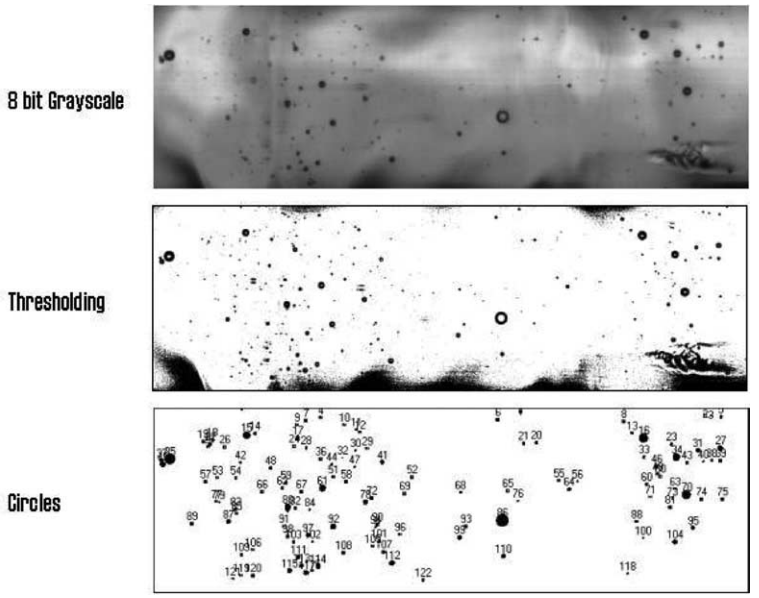

Fig. 3. Image processing steps for base film ROI.

filtered out, only the significant circular contours remain. A final step in the processing counted and sized the circles, as shown in the third image. Since the liquid films in the annular regime were so thin, bubble overlap was infrequent and was neglected in the image processing. An output file in spreadsheet format was generated containing all the information that resulted from the batch processing of the 100 images at each flow condition in the experimental matrix.

The base film is predominantly smooth and provides good contrast for bubble contour detection. However, when a disturbance wave appears in the ROI, the increased film thickness and interfacial roughness scatter most of the light and contrast is poor. The increased thickness also allows for substantial bubble overlap. Recently entrained bubbles within disturbance waves were also larger and appeared deformed by shear, which made them unfit for detection using the Heywood criterion. Most of the bubbles that were present in disturbance wave frames were not detected, as shown by the evolution of the image processing in Fig. 4. Even though multiple relatively large bubbles are visible in the grayscale image, the image processing detects a single bubble. Consequently, the concentration data reported below underestimate the total number of bubbles since the image processing script did not have the capability of differentiating between disturbance wave images and base film images.

However, disturbance waves represent only a small portion of the total images of a given dataset. Assuming that frames with less than 30% of the average bubble concentration were disturbance wave frames, it was determined from several sets of 100 images along the side of the tube that less than 5% of the images contained disturbance waves. Moreover, using wave spacing data obtained by Schubring and Shedd (2004), and using a conservative estimate for the length of tube affected by a single interfacial wave (1 cm), it was found that the area affected by interfacial waves, represents between 4% and 6% of the total area. Furthermore, the rather large bubbles

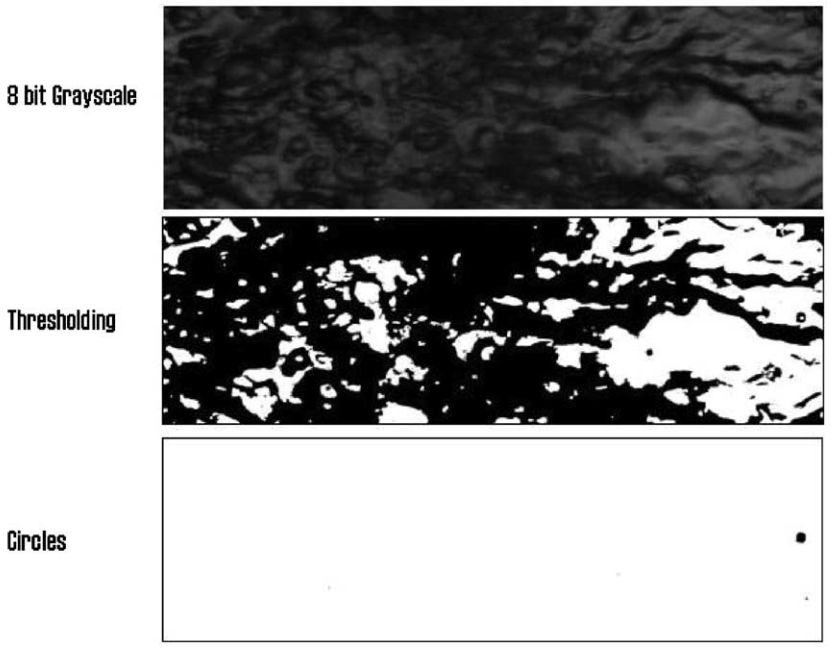

Fig. 4. Image processing steps for disturbance wave ROI.

observed within disturbance waves quickly break up into smaller bubbles. Thus, the statistical data presented below represent the size distribution of entrained bubbles within the base film that exists between the passage of disturbance waves.

2.5. Bubble size uncertainty

Several sources of uncertainty exist when extracting quantitative data from images. In this application, the uncertainty falls primarily into two categories: size distortion due to the imaging optics and illumination system, and alterations to the original image due to the image processing. The uncertainty in the diameter measurement due to the illumination system is believed to be smaller than a pixel. This is based on the fact that for particles of this size illuminated by diffuse, visible light, diffraction of light around bubble edges will produce only small variations in intensity. In addition, parallax and tube curvature distortions are minimized by restricting data analysis to about the center third of the image. Finally, manual comparison between images obtained using the backlit method and images obtained by reflection of light from the bubble surfaces resulted in consistent bubble measurement statistics.

The camera was focused on the inside wall surface prior to each set of runs using backlit droplets at rest on the wall. Since the liquid film in the present study is never more than 0.5 mm thick, which is about the depth of field of the lens system, the bubbles are assumed to be in focus at all times. However, the bubbles flow with a velocity of about 0.5–0.9 m/s (Kopplin, 2003) and the flash lamp pulse width is approximately 30 μs, so a bubble in the liquid film may travel about 27 μm, or nearly 7 pixels, during the image exposure. The light intensity distribution is approximately Gaussian in

time, so the resulting image contains a rapidly decreasing blur to the front and rear (upstream and downstream) of the bubble of about 2–3 pixels. This blur was consistently eliminated during the thresholding processes described above.

Essentially, only the thresholding steps in the image processing algorithm have the potential to introduce additional uncertainty. These processes generally followed the recommendations of Kim and Kim (1994) and Lee et al. (1991) to determine the threshold values that would generate the best value of contrast (VC). In doing so, the motion blur was generally eliminated. According to Koh et al. (2001), the resulting processed images should give bubble diameters with an uncertainty of between 5% and 10% of the measured diameter. The optical dispersion effects tend to widen the bubble contour inward. Thus, the outer edge of the contour still corresponds to the outer edge of the bubble from dispersion considerations alone. However, the outer edge is also slightly widened outward by diffraction. Varying amounts of the contour width appear in the final binary image depending on the values used for the threshold that produces it. The measurement of the contour diameter was taken based on the best fit circle to the binary image of the outer edge of the contour. Consequently, the uncertainty is likely to be biased so that the bubble size is overestimated.

3. Results

3.1. Bubble size distribution

Fig. 5 shows typical examples of bubble size distributions observed along the side of the tube. Notice that the bubble diameters were normalized using the liquid film thickness, δ. The probability density distribution function, f, was defined so that the ordinate of each datapoint in Fig. 5 corresponds to the number of observed bubbles per bin divided by the total number of observed bubbles. The total area, A_{tot}, used for normalizing the bubble counts was the area represented by a single observation frame, A, multiplied by 100 (i.e., $A_{\text{tot}} = 100\ A$). The initial bubble count was performed using equally sized bins with units of pixels. However, the reported bin size $\Delta(D/\delta)$ is not the same for all the distributions since the film thickness observed for each flow setting (obtained from Schubring and Shedd, 2004) was used to normalize the diameter, D, in the abscissa as D/δ. The magnification factor of 4.2 μm/pixel was used to convert the bubble diameters in pixels to actual length units.

An exponential fit characterizes the probability density function via two parameters:

$$f = E\mathrm{e}^{-b(D/\delta)} \tag{1}$$

Thus, E is a dimensionless entrainment parameter that is proportional to the total bubble count and b is the power-law exponent for the distribution. The value of the power-law exponent is always positive; increasing exponent values indicate increasing breakup, since this shifts the size distribution toward smaller radii. The behavior of the power-law exponent along the top, side and bottom of the tube for the entire experimental matrix is presented in Fig. 6.

At the lowest liquid flow rates, as dryout was approached, b exhibited its highest values and very high sensitivity to increasing liquid flow rates. The behavior of b was very similar for the top, side and bottom locations, exhibiting noticeable dependence upon air flow rate and seemingly no dependence on water flow rate except near dryout. The general trend indicates that increasing the

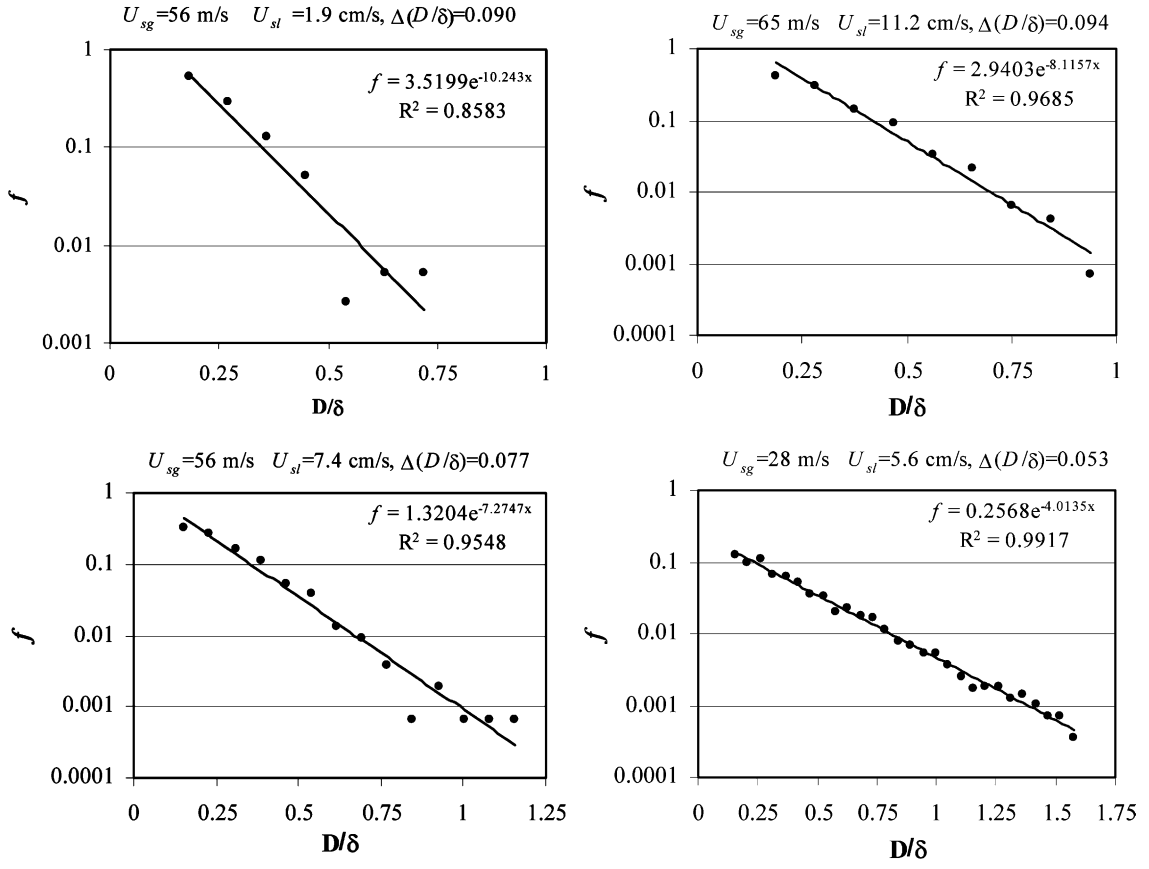

Fig. 5. Exponential fits to bubble size distributions.

air flow rate yields an increasing power-law exponent. The physical meaning of this change in the exponent is that the size distribution shifts toward smaller diameters as air flow increases.

Preliminary measurements performed using a lower resolution camera suggested the existence of a peak in the size distribution precisely at the second bin of the histogram. Using the higher resolution setup described above, it was evident that no such peak existed for that particular size since the observation of even smaller bubble diameters (made possible by the increased resolution) yielded even larger amounts of bubbles per bin for smaller diameters. The operation of the image processing filter that discards contours consisting of less than 20 pixels generated a false peak in the size distribution. For this reason, the first bin for every dataset was discarded before fitting the distribution to an exponential. The higher resolution results showed that the size distribution is monotonic and exponential, with the largest number of bubbles to be found in the smallest diameter bin of the histogram.

3.2. Mean bubble diameter

The arithmetic mean bubble diameter, $\overline{D}$, ranges between 12 and 26 μm. When normalized using the film thickness, $(\overline{D}/\delta)$, the mean bubble diameter ranges between 15% and 45% of the film

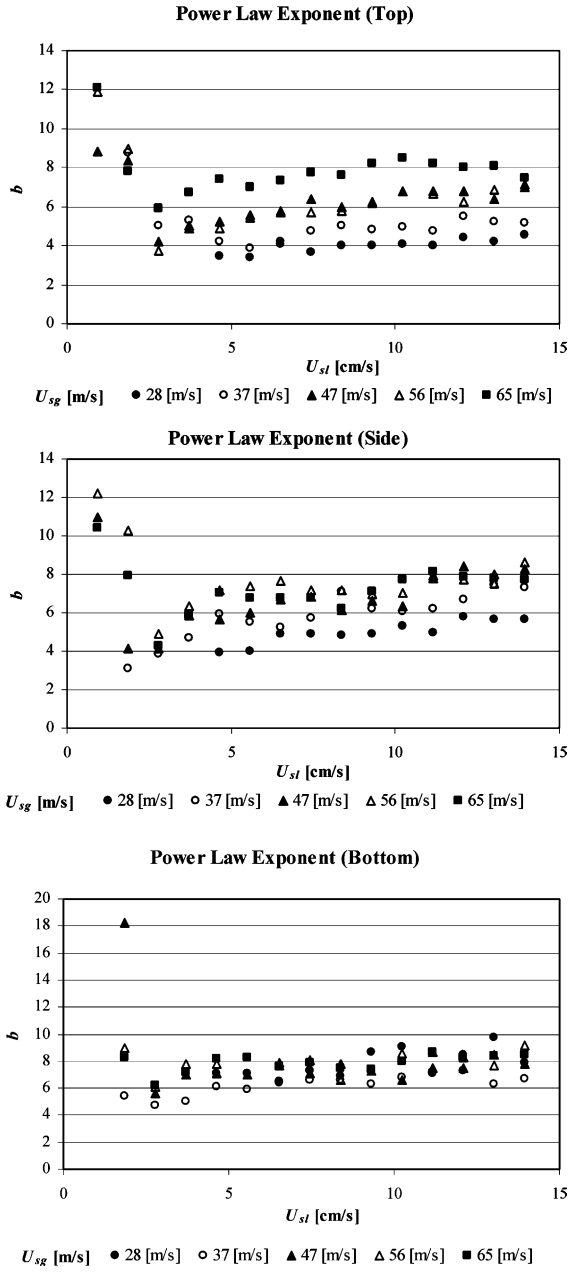

Fig. 6. Power-law exponent.

thickness as shown by Fig. 7. Away from dryout, no strong dependence on water flow rate is observed. Air flow rate dependence is evident along the bottom of the tube. The air flow rate dependence appears to be weaker along the top of the tube with most of bubble diameters ranging between 30% and 35% of the film thickness.

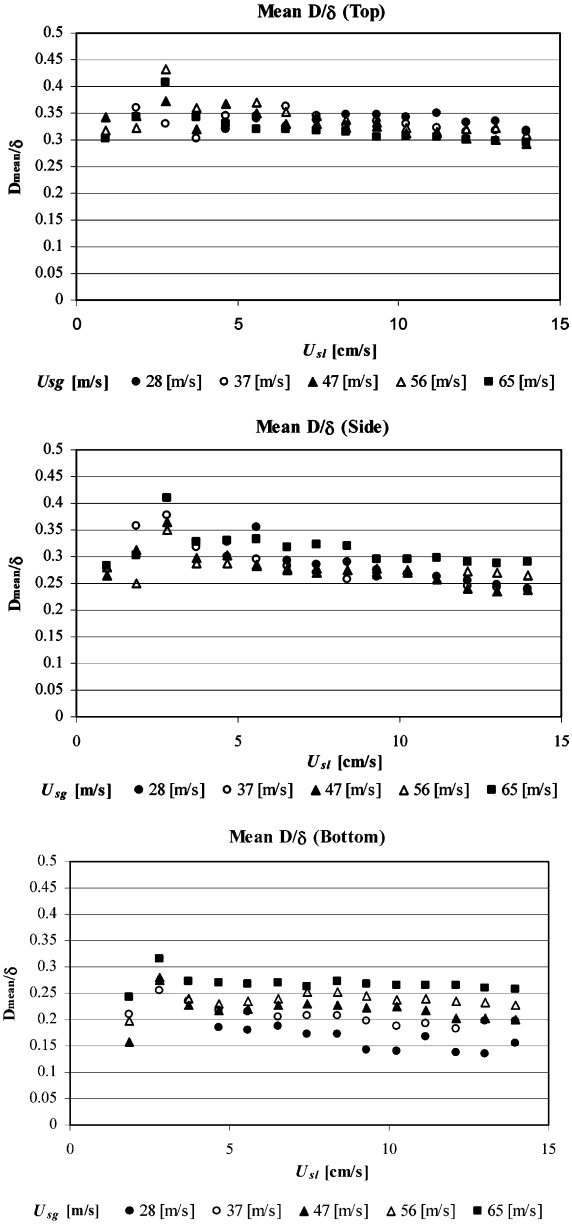

Fig. 7. Mean diameter divided by film thickness.

3.3. Bubble number concentration

The bubble number concentration, presented in Fig. 8, does not exhibit a clear trend for air flow rate dependence, although a range of variation of an order of magnitude is observed among the data. The total detected number of bubbles divided by the total area studied for each

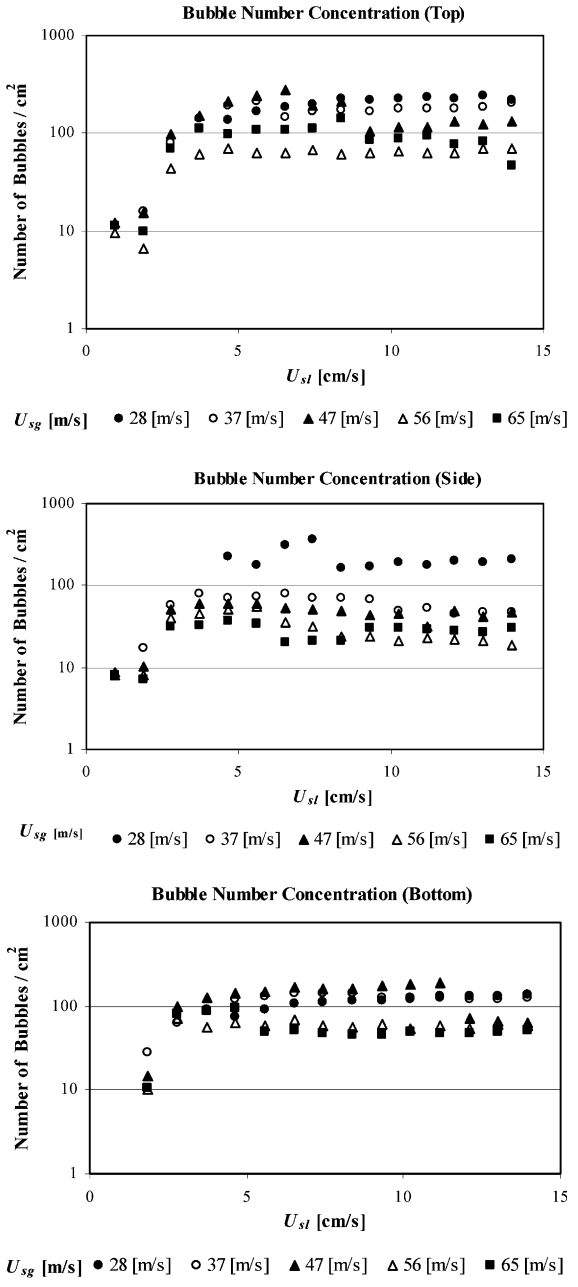

Fig. 8. Bubble number concentration.

distribution is not necessarily a perfect indicator of bubble concentration in the base film due to the presence of disturbance wave frames, as discussed earlier. Also, the image processing algorithm is not perfect, so some bubbles were missed. Thus, the bubble count underestimates the actual bubble concentration. There is a large reduction in the number of bubbles in the last panel

of Fig. 8 for $U_{sg} = 47$ m/s and large liquid velocities. No changes in flow conditions, imaging or other reasonable explanations were found for this change in behavior for this particular set of data.

4. Discussion

4.1. Entrainment mechanisms

The behavior of the power-law exponent, i.e., decreasing with increasing air flow, suggests that the bubble size distribution strongly depends on the flow mechanics. From the observations made in the present study, it is proposed that the dominant mechanism is a continuous folding action within the disturbance waves that entrains relatively large bubbles that break up quickly. The folding action mechanism remains a speculation until more cross cut images are studied in detail. However, the authors believe that entrainment caused by disturbance waves may be a scaled down version of the hydraulic jump air entrainment documented in Chapter 7 of Chanson (1996) and the references within it.

The bubble distribution that exists in the base film in between disturbance waves is likely to be the result of break up and subsequent turbulent mixing that spreads apart bubble clusters resulting from the breakup of large bubbles. Evidence of these processes may be seen in the backlit images and cross cut images obtained using Pulsed Laser Induced Fluorescence (PLIF) (Rodríguez and Shedd, 2004) shown in Fig. 9. Fig. 10 shows a schematic of the setup used for the PLIF images. The laser light sheet is used to excite a fluorescent dye in the liquid. The peak wavelength of the fluorescence is larger than the excitation wavelength of the laser, and thus the long pass filter allows the camera to capture only the light coming from the cross cut through the liquid while stray reflections from the laser sheet are eliminated.

The cross cut images, shown on the left, each present an axial slice that is about 0.5 mm thick (into the page) and 5 mm long (in the flow direction) of a typical wave on the liquid film. These images clearly document the entrainment of large bubbles by waves and show how the nature and size of waves change as the air flow rate increases. At lower superficial gas velocities ($U_{sg} = 28$ and 37 m/s), waves are similar to roll waves and larger in size, and many large bubbles are entrained by them. The higher superficial gas velocities ($U_{sg} = 47$–65 m/s) produce disturbance waves that, unlike the roll waves, appear to travel as separate entities on top of the base film; fewer and smaller bubbles are entrained by them. Changes in liquid flow rate do not produce significant changes in wave nature or size (the additional liquid is carried by additional waves, as frequency and wave velocity increase as documented by Schubring and Shedd (2004)). The backlit images in Fig. 9, corresponding to the same flow conditions of each wave image on the left, show how the bubble size distribution changes within the base film between disturbance waves. In agreement with the results for the power law exponent and mean radius (Figs. 6 and 7), the distribution shifts towards smaller sizes as air flow rate increases.

The most striking feature of the bubble number concentration results is that the most bubbles are entrained for the lowest gas superficial velocity. This may be connected, at least in a speculative manner due to the limited amount of cross cut images presented here, to the nature of the disturbance waves shown in Fig. 9. The total entrained gas volume is larger for the wave observed at the lowest gas superficial velocity; this may ultimately produce a higher bubble number

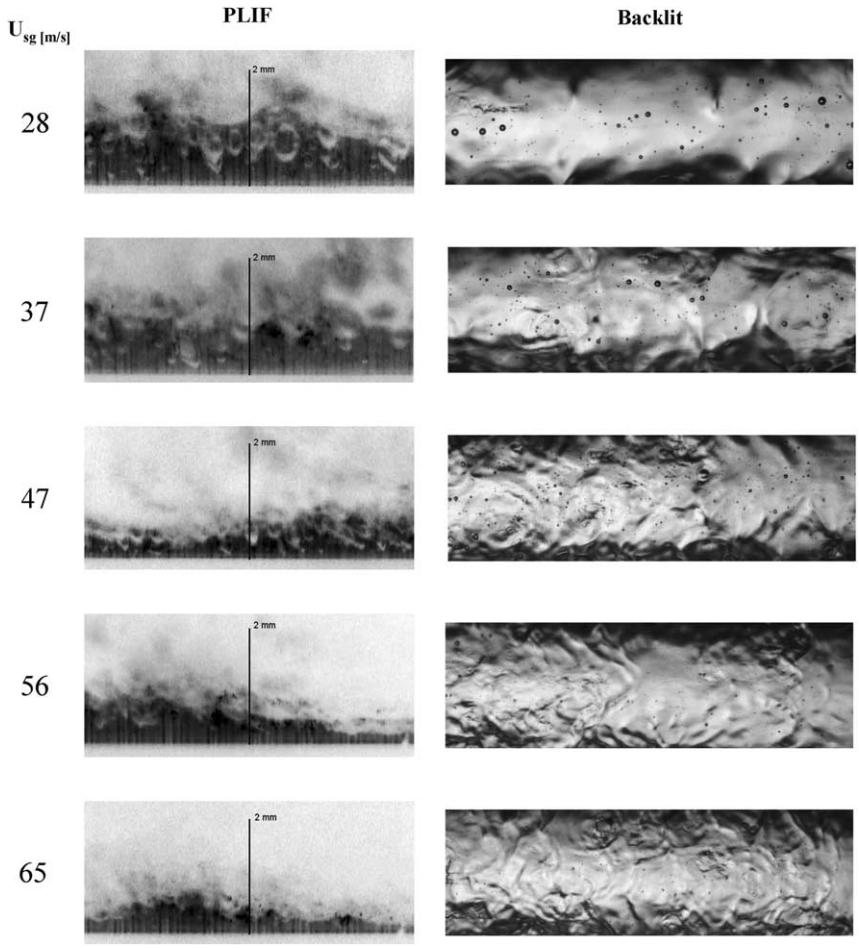

Fig. 9. PLIF images of disturbance waves (left) and backlit images of base film (right) for increasing U_{sg}. Backlit images represent a 12.5×3.9 mm area. All images depict the bottom of the tube for $U_{sl} = 9.3$ cm/s. The two parallel sets of data correspond to separate experimental runs. Flow from right to left.

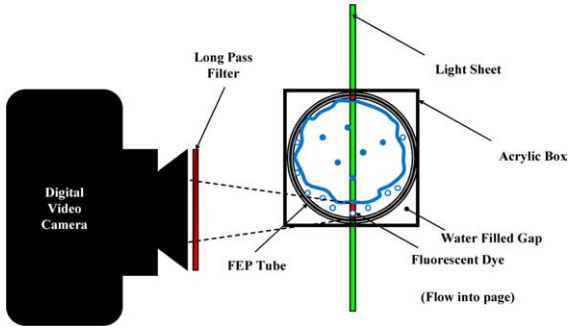

Fig. 10. Schematic of setup for PLIF images along the bottom of the tube.

concentration in the base film. Even if the wave frequency increases for the higher gas superficial velocities, this does not appear to compensate for the reduction in the volume of gas entrained by each individual disturbance wave. See Rodríguez and Shedd (2004) for a more detailed discussion of the mechanism of gas entrainment by waves.

Droplet impacts and bursting bubbles are known to generate small bubbles in a thin film (Mesler, 1976). Although the existence of these events is acknowledged by the authors, this type of entrainment was not clearly documented by the visualization techniques and the image processing used in the present study. It is possible that these mechanisms may contribute to the total entrainment, particularly at the higher air flow rates where a mist flow condition may exist in the gas core. This could be an explanation for the bubble number concentration to increase at $U_{sg} = 65$ m/s, while it decreases as U_{sg} varies from 28 m/s to 56 m/s as shown in Fig. 8. The contribution of droplet impacts to total bubble entrainment appears to be a secondary effect, as this behavior would be expected to show a stronger dependence on liquid flow rate. In addition, if droplet impacts were a significant source of entrainment at the lower superficial gas velocities, higher concentrations would be expected towards the bottom of the tube since gravity is important when compared to inertia at the lower gas flow rates. This increased concentration at the bottom is not observed in the bubble number concentration data.

4.2. Bubble breakup

Increasing the gas flow rate produces higher exponent values, as shown in Fig. 6, which translates into distributions with a larger amount of small bubbles. From the data presented, it appears that elevated interfacial shear promotes the breakup of the larger bubbles in the distribution. On the other hand, the power-law exponent remains fairly constant as liquid flow rate changes.

Measurements of the liquid film thickness between disturbance waves are shown in Fig. 11. The base film thickness remains nearly constant at the higher gas flow rates, suggesting that an

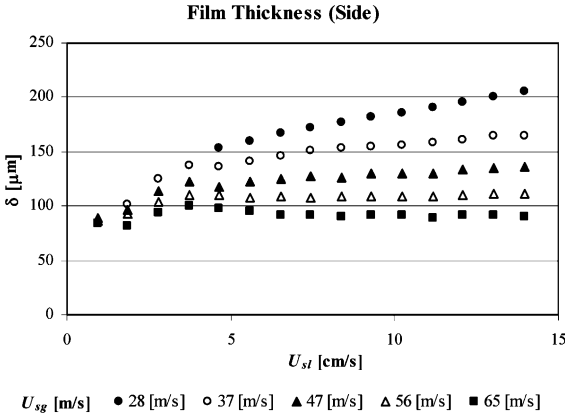

Fig. 11. Base film thickness along the side of the tube measured by Schubring and Shedd (2004) using optical method developed by Shedd and Newell (1998).

increment in liquid flow rate will increase the disturbance wave frequency through the generation of more waves. This has been documented for these flows using a non-intrusive total internal reflection optical sensor (Shedd and Newell, 1998; Schubring and Shedd, 2004). The relative independence of bubble entrainment with respect to liquid flow rate in the annular regime appears to be related to the fact that disturbance wave velocities are a strong function of air flow rate, but a much weaker function of liquid flow rate. The film thickness data also suggest that, once a bubble escapes the disturbance wave and remains in the base film, it will experience nearly constant shear forces regardless of the liquid flow rate over the range studied. As observed in the last panel of Fig. 5, the largest bubbles in the base film can be even larger than the mean film thickness. These bubbles are unlikely to survive at such a size very long.

The data suggest, then, that gas is entrained in a random manner by trapping and folding at the gas/liquid interface of a disturbance wave. These bubbles are then broken up under shear between the fast moving wave and the wall. We have found that the critical Weber number,

$$We_c = \frac{\rho_l (U_{dw})^2 D_{max}}{\sigma}, \tag{2}$$

based on the mean disturbance wave velocity, U_{dw}, liquid density, ρ_l, surface tension, σ, and maximum bubble diameter, D_{max}, attains a value between 40 and 100 for the majority of data measured at $U_{sg} = 37$ m/s and higher and superficial liquid velocities, U_{sl}, greater than 0.05 m/s. A notable exception occurs for the two lower gas flow rates along the bottom of the tube, where values of We_c between 100 and 140 are observed. We_c for the lower liquid flow rates is typically lower than 40. Fig. 12 shows values of We_c calculated using values of U_{dw} from Schubring and Shedd (2004) and values of D_{max} from the present study. Weber numbers based on other characteristic velocities do not appear to correlate the data at all.

4.3. Exponential size distribution

The exponential distribution of bubble sizes has been observed in other studies of bubble entrainment due to waves on large bodies of water. Deane and Stokes (2002) found that bubbles entrained by breaking ocean waves followed exponential trends with exponents of 10/3 for bubbles with radii between 1 and 10 mm and 3/2 for bubbles between 0.1 and 1 mm. Although they did not present a large amount of data for bubbles smaller than this, it appears that the exponent would decrease again for bubbles with radii below 0.1 mm. Thus, the shape of the size distribution obtained in the present study is consistent with this previous work, although the change in exponent indicates that the shearing mechanisms in annular flow differ from those in breaking ocean waves. For the Dean and Stokes situation, the critical Weber number is 4.7 and the critical Reynolds number is 450 (both based on the turbulent velocity fluctuation component at the scale of the bubble). Those critical numbers essentially describe a breakup mechanism directly associated with turbulence at the scale of the bubbles; they are thus much smaller than critical numbers based on the disturbance wave velocity. In the present study, the breakup mechanism is probably different; it is more likely to be associated with the disturbance wave velocity and the velocity gradient that exists across the film thickness.

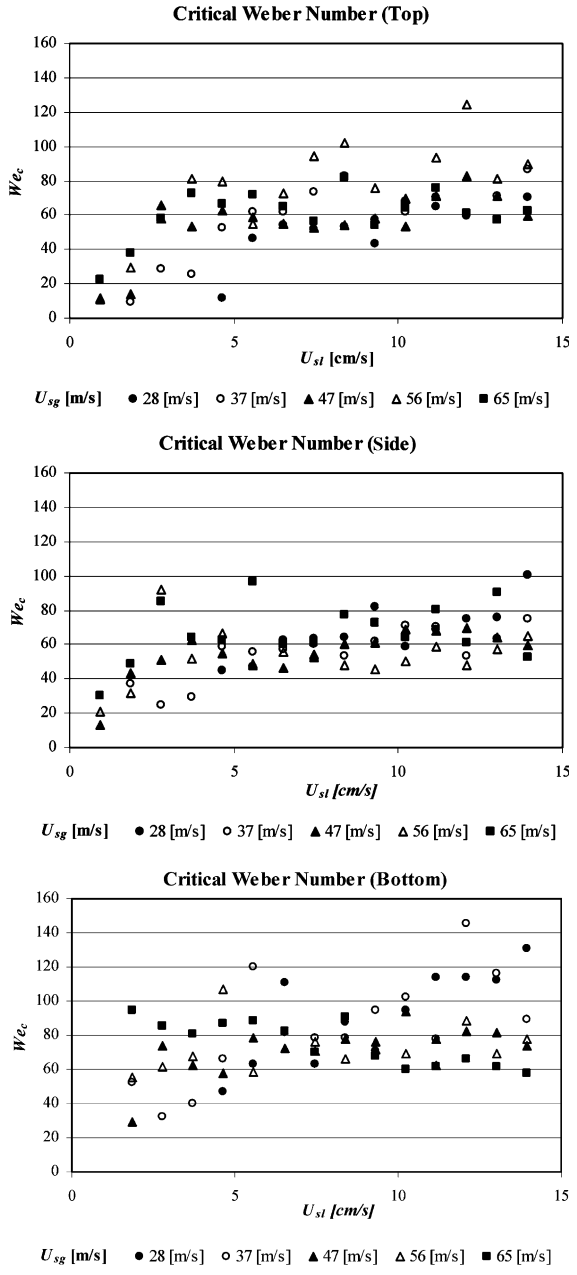

Fig. 12. Critical Weber number.

5. Conclusions

- A clear association has been established between disturbance wave action and bubble entrainment in the liquid film of horizontal annular flow. Bubble breakup is also linked to the flow

mechanics as indicated by the behavior of the power-law exponent.
- Bubble statistics show strong dependence on air flow rate, but only a weak influence of liquid flow rate over the flow conditions studied. This behavior may be explained by the fact that air flow rate determines the velocity, size and nature of waves (i.e., disturbance or roll waves).
- Liquid flow determines disturbance wave frequency but does not affect the bubble distribution.
- The consistent values of the critical Weber number based on mean disturbance wave velocity confirm the association between wave action and bubble breakup for flow settings where dry-out was not imminent.

Acknowledgements

The authors appreciate the financial support for this project provided by the University of Wisconsin-Madison and the National Science Foundation under award number CTS-0134510. The authors thank Prof. S.A. Klein for many helpful discussions.

References

Arnold, C.R., Hewitt, G.F., 1967. Further developments in the photography of two-phase gas–liquid flow. J. Photograp. Sci. 15, 97–114.

Chanson, H., 1996. Air bubble entrainment in free-surface turbulent shear flows, first ed. Academic Press, London.

Cooper, K.D., Hewitt, G.F., Pinchin, B., 1964. Photography of two-phase gas/liquid flow. J. Photograph. Sci. 12, 269–278.

Deane, G.B., Stokes, M.D., 2002. Scale dependence of bubble creating mechanisms in breaking waves. Nature 418, 839–844.

Gonzalez, R.C., Woods, R.E., 1993. Digital Image Processing, first ed. Addison-Wesley Publishing Company.

Hewitt, G.F., Jayanti, S., Hope, C.B., 1990. Structure of thin liquid films in gas–liquid horizontal flow. Int. J. Multiphase Flow 16, 951–957.

Jacowitz, L.A., Brodkey R.S., 1964. An analysis of geometry and pressure drop for the horizontal, annular, two-phase flow of water and air in the entrance region of a pipe. Chem. Eng. Sci. 19, 261–274.

Kim, K.S., Kim, S.S., 1994. Drop sizing and depth-of-field correction in TV imaging. Atomizat. Sprays 4, 65–78.

Koh, K.U., Kim, J.Y., Lee, S.Y., 2001. Determination of in-focus criteria an depth of field in image processing of spray particles. Atomizat. Sprays 11, 317–333.

Kopplin, C.R., 2003. Local liquid velocities in horizontal, annular air/water flow. In: Proceedings of 2003 ASME International Mechanical Engineering Congress & Exposition, IMECE2003-43595.

Lee, S.Y., Park, B.S., Kim, I.G., 1991. Gray level factors used in image processing of two-dimensional drop images. Atomizat. Sprays 1, 389–400.

Mesler, R., 1976. A mechanism supported by extensive experimental evidence to explain high heat fluxes observed during nucleate boiling. AIChE J. 22, 246–252.

Mesler, R., 1977. An alternative to the Dengler and Addoms convection concept of forced convection boiling heat transfer. AIChE J. 23, 448–453.

Rodríguez, D.R., Shedd, T.A., 2004. Cross-cut images of the liquid film in air/water horizontal annular flow. 2004 ASME Heat Transfer/Fluids Engineering Summer Conference, Charlotte, NC, July 25–29.

Schubring, D., Shedd, T.A., 2004. Detailed characterization of two-phase annular flow in a horizontal tube. 2004 ASME Heat Transfer/Fluids Engineering Summer Conference, Charlotte, NC, July 25–29.

Shedd, T.A., Newell, T.A., 1998. Automated optical liquid film thickness measurement method. Rev. Sci. Instr. 69 (12), 4205–4213.

Sun, G., Hewitt, G.F., 2001. Evaporation and condensation of steam-water in a vertical tube. Nucl. Eng. Design 207, 137–145.

Thome, J.R., 1995. Flow boiling in horizontal tubes: A critical assessment of current methodologies. In: Proceedings of the Symposium on Two-Phase Flow Modelling and Experimentation, Rome, Italy, pp. 41–52.

Thorncroft, G.E., Klausner, J.F., 1997. A capacitance sensor for two-phase liquid film thickness measurements in a square duct. ASME J. Fluids Eng. 119, 164–169.